The Simulated Response of Detached Tokamak Edge Plasma to Transient Heat-Bursts

C. T. Aird[1]

[1]Department of Physics, The University of York, York, YO10 5DD, United Kingdom

December 9, 2025

Abstract

Divertor detachment is key to the handling of power-loads within fusion reactors. However, Tokamak edge-regions are regularly subjected to strong bursts of heat from the plasma core. Detailed investigation into the response of a detached divertor to the onset of these heat-pulses has yet to be carried out. This report presents an analysis of this response through the use of a 1D plasma-fluid code. Rapid divertor re-attachment was found to produce high amplitude sound waves originating in front of the target and travelling upstream. Furthermore, the deposition of energy far above that contained within the pulse was observed. This was a result of the transfer of energy flow from radiative losses to target heat-flux. Increasing upstream density was found to increase this effect on both MAST-U and ITER. Additionally, expanding the magnetic flux area close to the target was found to both reduce Divertor heat-loads, in proportion to the expansion in area, and better maintain radiative losses. Thus, an overall more robust divertor was produced. Additionally, target heat-loads scaled linearly with the background energy entering the edge-region. These observation have several implications. For a detached divertor, there is a limit to the size (power and duration) an ELM can reach before the Divertor re-attaches. Once this occurs, an increased volume of energy would be deposited on the target. Furthermore, Physical measurements of target heat-loads may overestimate the energy expelled from the core plasma during ELM transients.

Contents

1 Introduction

Magnetic confinement fusion (MCF) aims to achieve a net output of energy through the fusion of Deuterium (D) and Tritium (T) in the reaction,

$$D + T \Rightarrow He + n + 17.6\ MeV$$

MCF does this by confining charged particles in the form of plasma, thus, minimising energy losses. The Tokamak (shown in Figure 1) is recognised as the optimal geometry for achieving this confinement. However, energy and particles still eventually leave the plasma core. Therefore, to prevent excessive damage to plasma facing components (PFCs), energy and particles must be quickly removed from the plasma edge. As described in the sections below, several techniques have been developed to achieve this. Even so, excessive power-loads within the edge region of Tokamak reactors remain a major obstacle to the production of net energy through fusion.

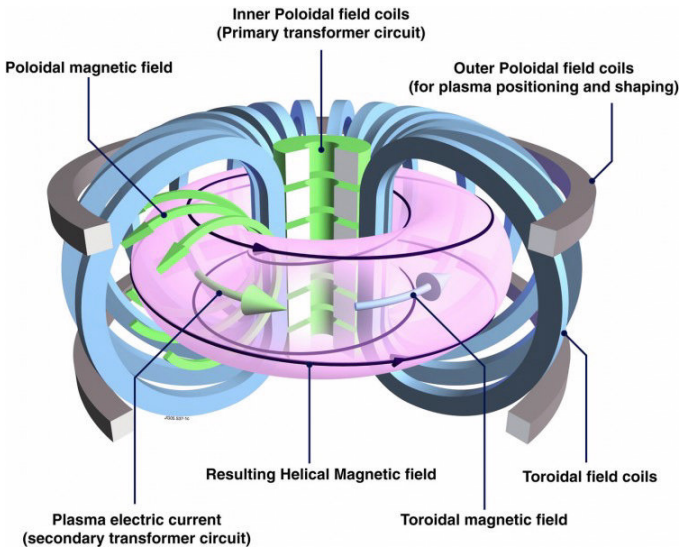

Figure 1. Diagram of a Tokamak, showing both toroidal and poloidal coils, the toroidal plasma and helical magnetic field. The inner poloidal field coils induce a current in the plasma which provides resistive heating and produces the confining poloidal field (Image source: eurofusion.org).

Advancements in Tokamak edge plasma technology, such as Divertor physics (see section 2.2), have greatly improved the power and particle control of Tokamaks within steady-state. However, transient modes now pose the biggest threat to MCF research. Promising operational modes of increased energy confinement have been discovered. Unfortunately, these modes are accompanied by undesirable eruptions of energy into the edge region. These eruptions, known as Edge-localised modes (ELMs), (depicted in Figure 2) are described within section 2.5. ELMs result in the rapid deposition of energy onto PFCs and can result in their melting or sublimation. Because of this, the development of detailed models of ELM-driven edge-plasma evolution and power-load mitigation methods are major goals of MCF research. Furthermore, these high-confinement modes are aided by additional edge-plasma states. Most notably, plasma detachment (see section 2.4) drastically aids power and particle control. Detachment sees the build-up of neutral gas in front of PFCs and helps to cushion against strong heat transfer. Consequently, future Tokamaks plan to operate within high confinement modes containing detached edge-plasma. However, little research has so far been carried out into the response of detached plasma to heat-pulses. For this reason, the work presented within this report formed an investigation into this response.

This report hopes to provide an answer to several questions relevant to the understanding of Heat-pulses, such as ELMs, within Tokamak reactors. Firstly, a key focus was to understand the processes effecting the deposition of pulse-energy onto PFCs. Furthermore, what sort of heat-loads can be expected within physical reactors such as MAST-U or ITER and, more importantly, how do the sizes of these pulses (power and duration) influence heat-loads? Another question to be answered was if the Super-X Divertor design, present on MAST-U [1], is worth the extra cost and complexity? To answer this question, the

impact of varying the magnetic flux expansion close to the target was to be tested. Finally, the affect of increasing the degree to which the divertor has detached was investigated.

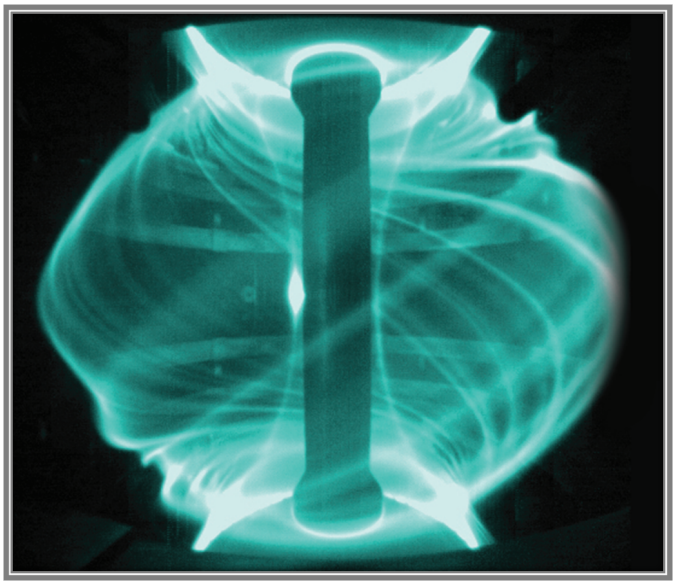

Figure 2. A high speed image of the MAST plasma during ELM eruption. ELMs can be seen as filaments twisting around the spherical shape (Image source: euro-fusion.org).

In Section 2, we begin by discussing the general physics behind many of the topics discussed in this report. In Section 3, we will move onto the program and methods used for data collection and validation. Then, results will be presented alongside some discussion of their relevance within Section 4 before conclusions are drawn within Section 5.

2 Theory

This Section will cover the physics most relevant to this investigation of Tokamak edge plasma. These will include the processes determining heat flow and loss within the edge, the various operational states of this region and its different designs.

2.1 SOL Heat Transport

Charged particles stick to solid surfaces long enough to allow recombination to occur. Surface recombination can deposit energy through two main effects. Firstly, assuming a hydrogenic plasma, 13.6 eV is deposited as an electron enters the ground state of the newly formed atom. Following this, atoms can combine to form molecules on the surface and deposit around 2.2 eV more [2]. Newly recombined neutrals can then back-scatter into the plasma to be ionised once again. This process is know as recycling. Since charged particles are re-released from the surface, an energy sink is formed but not a mass sink. Thus, conduction is a permitted mechanism of energy transport in plasma sink action.

To implement plasma sink action, a solid surface (target) must be placed across open field lines, forming a scrape-off layer (SOL) beyond the separatrix (last closed magnetic field line). The initial presence of a particle sink accelerates plasma towards the target. Due to their reduced mass, electrons rush ahead of ions in the first few μs. A negative charge builds up on the solid surface forming a potential between the plasma and the target. This potential slows electron loss but increases ion loss. The formation of a debye sheath shields the bulk plasma from most of this negative charge. However, a small field penetrates upstream, further diverting ions to the target.

The heat sink coupled with the ion diverting field helps to protect most PFCs. However, another problem arises from the use of a solid target. The competition between poloidal and the much slower perpendicular (to the magnetic field, $\mathbf{B}$) transport leads to a very small plasma 'wetted' surface area [3]. Poloidal transport is a combination of sink action, motion parallel to $\mathbf{B}$ and various particle drifts. In contrast, perpendicular transport results from drifts and turbulence alone. Provided the plasma is sheath limited (see below), parallel particle motion dominates the transport of heat in the SOL. Therefore, heat carried by particles will cover a large poloidal distance before travelling far across field lines. Unfortunately, this results in a thin SOL width ($\sim cm$) [4] and small target areas over which extreme heat-loads are deposited.

Strong particle flow is not always necessary for the transport of heat in the SOL. If there exists a high plasma density in the SOL, a transition from sheath-limited to conduction-limited heat transfer occurs. In a sheath-limited plasma little to no temperature gradients exist along the SOL. Therefore, the heat flow along this region is determined by the rate of heat transfer across the sheath in front of the target. Whereas, in a conduction-limited plasma, large temperature gradients are present and the heat conduction rate determines SOL heat transport. A transition to a conduction-limited plasma can be understood as the reduction of particle mean-free paths (λ) due to the increased plasma density.

2.2 Limiters and Divertors

So far, two key target designs have been used within Tokamaks - Limiters and Divertors. A Limiter is formed by simply placing the solid target through field lines just beyond the separatrix. Limiters are successful in producing sink action and heat removal. However, they have a drawback in the form of impurity emission. Impurities are released from Limiter surfaces through mechanisms such as sputtering and ablation [2]. The close proximity of Limiter targets to the bulk plasma allows these impurities to easily migrate across the separatrix and into the plasma core. This can be detrimental to reactor performance as prolonged operation may result in impurity-driven radiative cooling [5]. Thus, Limiters tend to be found on older machines and have lost the focus of MCF research.

The Divertor design offers a solution to the issue of impurity contamination. The Divertor region is situated away from the core plasma and linked via an additional coil, carrying a current I_D (Depicted in Figure 3). In the Divertor design, the target is placed such that it cuts through the magnetic flux surfaces surrounding I_D. Now, particles entering the SOL travel away from the bulk plasma to the Divertor region, where active pumping can remove impurities released from the target [6]. With this, it is clear that the Divertor design, along with active pumping, greatly reduces the risk of impurity contamination.

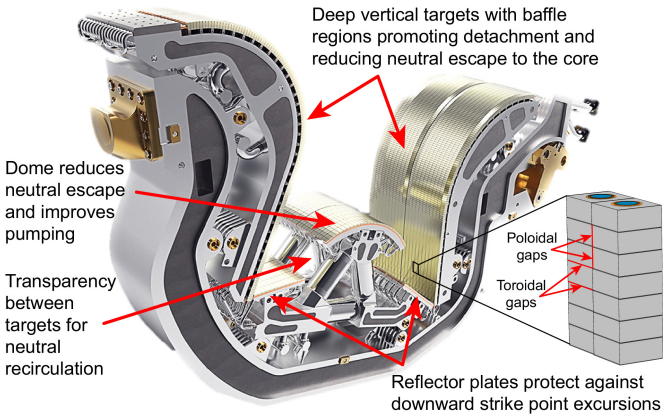

Figure 3. A CAD representation of a single ITER W Divertor cassette highlighting some key physics features of the design. Many of the features present in this design highlight the complexity of the Divertor and its influence on the neutral fluid and Divertor detachment (see section 2.4). This image has been taken from [7].

2.3 Mechanisms of Heat Loss

Once heat has been transferred along the SOL it must be removed from the system. There are several ways in which this energy can be lost within the SOL. Heat can be deposited directly onto surfaces such as the Divertor target. This happens through two processes, the simple transfer of thermal energy due to collisions and the more complex surface recombination described in section 2.1. In an ideal scenario this sort of heat loss would be minimised. Therefore, energy must be removed through other channels. Fortunately, several exist. Notably, radiative heat losses in the edge plasma are proving a useful mechanism of target heat-load reduction. It has been determined by H. Kubo *et al* [8] that impurity radiation in the SOL is a key mechanism by which energy, originally carried by ions to the target, is lost in the Divertor. If target energy-loads resulting from a heat-pulse are to be analysed, the various mechanisms of heat loss in the SOL must be understood.

Energy carried by the SOL plasma can be passed to neutral particles, for example through plasma-neutral collisions. However, this form of energy transfer does not remove the heat from the system but simply stores it within the neutral fluid. Other than deposition onto solid surfaces, there is only one other way in which energy can be lost from the system - the emission of radiation. On top of impurity radiation, a number of processes contribute to the total radiative losses in the SOL. Ion-neutral interactions such as excitation, charge exchange and ionisation result in the emission of radiation. Additionally, the recombination of ions and electrons further contributes to these losses. It has been well established that these processes take place within the Tokamak edge region and, in fact, play key roles in the resultant state of the system [9, 5]. Therefore, it is important to understand how the rate of each of these emission mechanisms varies with the plasma state; this is shown in Figure 8.

The deposition of energy onto target surfaces tends to be the dominant mechanism of heat loss within the SOL. However, these target heat-loads must be kept to acceptable levels to allow extended reactor lifetimes. Multiple ways of characterising heat-loads have been suggested. Some of these include the total heat-flux incident on Divertor targets ($q_{||,t}$) [10] and $\Delta E/\sqrt{t}$, where ΔE is the energy density deposited on a target surface in a time interval, t. For both of these quantities there exists damage defining thresholds. For actively cooled structures, $q_{||,t} \leq 10\ MWm^{-2}$ would result in acceptable Divertor lifetimes. However, during transients ($\sim 0.1\ ms$), this limit is increased to 20 MWm^{-2}. In contrast, most thresholds in units of $\Delta E/\sqrt{t}$ are much more strict and define points beyond which a change of state can occur, such as melting ($40\ MJm^{-2}s^{-1/2}$) or sublimation ($\sim 45 - 50\ MJm^{-2}s^{-1/2}$) [3]. It should also be noted that Divertor lifetimes may be reduced significantly with high values of $\Delta E/\sqrt{t}$, even below a change of state threshold. Due to the transient nature of the heat-pulses simulated throughout this investigation, $\Delta E/\sqrt{t}$ is a more relevant quantity for defining heat-loads.

2.4 Detachment

Several strategies have been employed in present day machines including JET [11], amongst others, to reduce Divertor target heat-loads. Poloidally inclining the Divertor targets and increasing the magnetic

flux expansion both act to maximize the area over which power is deposited. However, a mode of operation known as detachment has shown particular improvement for target heat-loads due to the increased level of radiative losses observed. This phenomenon of detachment sees the plasma edge, at which boundary conditions apply, appear to move upstream away from target surfaces. In fact, what is actually happening is a build up of neutral gas in front of the target, which was first demonstrated by Hsu *et al* in 1982 [12]. Hsu forced detachment by puffing gas into the the Divertor region. However, before Divertor detachment can occur, the edge plasma must enter a high-recycling (HR) regime.

The HR regime was first observed by F. Alladio *et al* in 1982 [13]. Characteristic of this regime is the short ionisation lengths present in front of the target. Consequently almost all neutral ionisation occurs close to the target, leading to high levels of recycling in the 'recycling region'. Thus, ionisation rates in the rest of the edge plasma reduce to near zero, resulting in no strong particle flow. Therefore, the plasma pressure is constant along open field lines and equal to upstream values (p_u). To sustain this pressure an effective pressure of the plasma-neutral mix in the recycling region builds up [14].

Although there is a lack of particle flow throughout the majority of the SOL during the HR regime, there is still a high plasma flux ($nv_{||}$) on target surfaces. The HR regime actually sees a rise in the target flux, $nv_{||,t}$, caused by the increased recycling rates. As the upstream plasma density (n_u) is increased, $nv_{||,t}$ continues to rise due to reduced λ values, ultimately increasing the rate of neutral recycling close to the target. However, beyond a limit, $nv_{||,t}$ 'rolls-over' and proceeds to decrease with increasing n_u [15]. This can be understood as a growth in Divertor emissivity, as shown in Figure 4. As λ further decreases, reaction rates continue to increase. However, it is now impurity radiation and volumetric plasma recombination rates which become important.

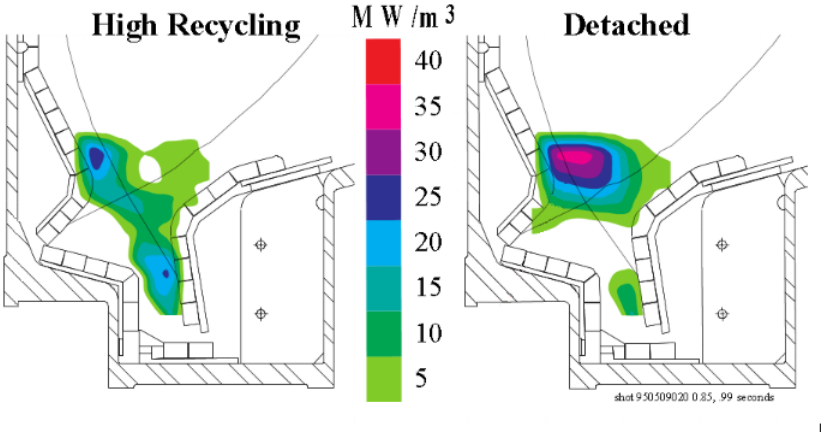

Figure 4. Evidence of increased Divertor emissivity during detachment [16]. This increase in radiation results in a reduction of $nv_{||,t}$, as the ion momentum is lost to the neutral gas cushion in front of the target.

To describe the transition from a HR plasma to a detached Divertor quantitatively, power balance along the SOL must be considered [17].

$$Q_{SOL} = Q_{imp} + Q_H + Q_{rec} + Q_w \tag{1}$$

Here, Q_{SOL} is the power-flux crossing the separatrix, into the SOL, Q_{imp} is the power-flux radiated away by impurities, Q_H the hydrogenic radiation loss, Q_{rec} the power lost to recombination within the SOL and Q_w represents the power-flux to walls and target surfaces. Several of these quantities can be linked to particle sources and sinks. For example, Q_H and Q_{rec} can be described in terms of an ion flux source (Γ_{ion}) and volumetric recombination sink (Γ_{rec}), respectively, with the energy 'cost' per ionisation (E_{ion}) or recombination (E_{rec}) event converting to units of power-flux.

$$Q_H = E_{ion}\Gamma_{ion}, \qquad Q_{rec} = E_{rec}\Gamma_{rec} \tag{2}$$

When combining equations (1) and (2) whilst assuming ion flux continuity in the SOL ($\Gamma_{ion} = \Gamma_w + \Gamma_{rec}$), an equation for the particle flux to PFCs (Γ_w) can be determined,

$$\Gamma_w = \frac{Q_{SOL} - Q_{imp} - \Gamma_{rec}(E_{ion} + E_{rec})}{E_{ion} + E_w} \tag{3}$$

Here, E_w is the energy transferred to PFCs by each particle impinging on them. E_w encompasses both the kinetic energy deposited and the energy transferred due to processes such as surface recombination. For HR and detached plasma, the temperature close to the target is relatively low ($\sim$ few eV). Therefore, the kinetic energy term in E_w is small. Thus, assuming the cost of ionisation is much greater than that associated with volumetric or surface recombination, (3) can be simplified to,

$$\Gamma_w = \frac{Q_{SOL} - Q_{imp}}{E_{ion}} - \Gamma_{rec} \tag{4}$$

To characterise Divertor detachment, two key measures can be taken. As shown in Figure 5 Divertor detachment sees a dramatic drop in pressure at the Divertor resulting in electron temperatures below 5 eV. Furthermore, Equation (4) shows that, for a constant Q_{SOL}, a reduction of plasma flux to target surfaces is only possible through an increase in impurity radiation or volumetric recombination. For these reasons, it can be said that the detachment of a Divertor plasma will be observed as sub 5 eV target electron temperatures and a rollover in target plasma flux caused by increased impurity and volumetric recombination-driven radiative losses.

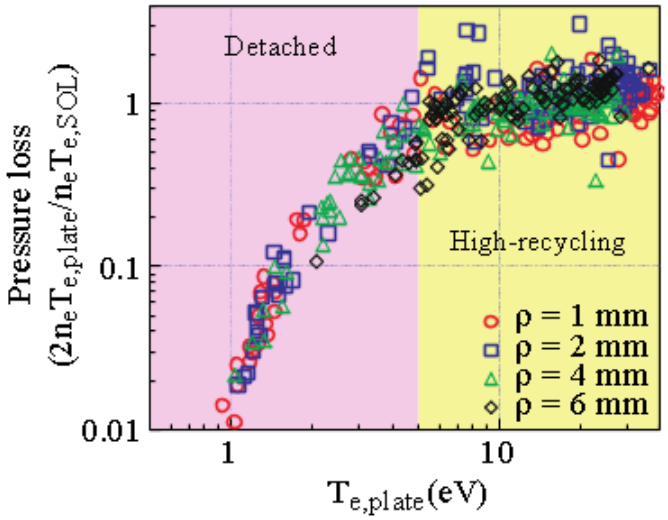

Figure 5. An attached SOL plasma demonstrates the halving of plasma pressure from upstream to the target. However, a dramatic loss in plasma pressure at the target, due to increased ion-momentum reducing collisions, forms a detached plasma. This occurs for target plate electron temperatures $(T_{E,plate})$ less than 5 eV [18].

2.5 Edge-localised Modes, ELMs

Thus far, our discussion has focused on steady-state operating scenarios. However, edge plasma is often subjected to transient bursts of heat, known as ELMs. ELMs are only observed in a regime of increased bulk plasma confinement known as H-mode ('H' for high confinement). H-mode, was first observed on ASDEX in 1982 [19]. Once a threshold power is reached a transition from L-mode (low confinement) to H-mode occurs, approximately doubling the energy confinement time and drastically increasing the core temperature and pressure. The increased confinement arises from sharp radial pressure gradients present in the SOL. Measurements of electron density and temperature have established that these gradients occur across a few centimeters beyond the separatrix [20]. The gradients act as a pedestal lifting plasma parameters in the core to much greater values, as shown in Figure 6. The specific cause of the L to H-mode transition is unknown, but is of little relevance in this report. The important point to understand is that H-mode dramatically increases the confinement of energy in the bulk plasma, which is undeniably a positive. For this reason, future MCF reactors such as ITER will aim to operate within H-mode.

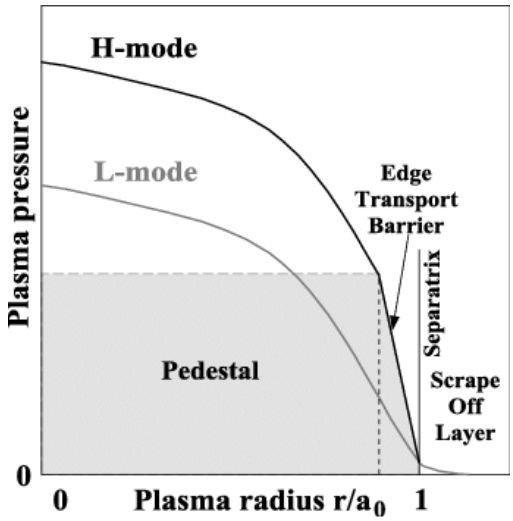

Figure 6. Typical radial pressure profiles for both L and H-mode plasma. a_0 is the radius from the plasma core to the separatrix.

However, H-mode also has it's drawbacks. The H-mode pedestal not only confines energy but also acts as a particle transport barrier. Consequently, impurity retention is increased within the core. The H-mode pedestal continues to grow until a limit is reached. At this point an ELM instability causes the rapid relaxation of the edge pressure, with a burst of heat and particles crossing the separatrix. After this ELM transients, the pedestal is re-established and the edge pressure builds towards the next ELM [21]. A single ELM can increase the target power-flux up to 60 MWm^{-2} on average [22] and can be detected as D_α signals similar to that of Figure 7. Despite the potential threat a rapid burst of heat into the edge region could pose, ELM-driven particle transport across the separatrix is a vital mechanism of impurity control within H-mode. Hence, ELM filled H-mode is the current planned initial operating scenario of the ITER reactor.

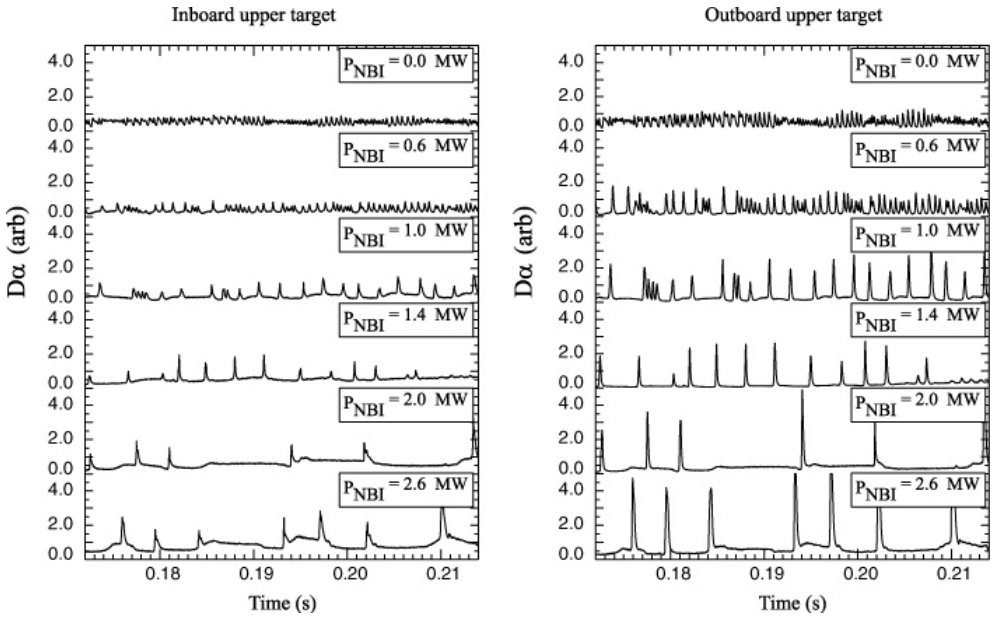

Figure 7. A D_α signal showing the variation of ELM frequency with increasing auxiliary heating power (P_{NBI}). An average pulse time of ~ 1.0 ms can also be seen. The terms stated above each graph refer to the locations of target plates where measurements were taken. This image was taken from [23].

3 Methodology

The methods described within this section where those used to produce the results shown in section 4. Additionally, some discussion of potential errors and limitations of the methods employed will be provided. However, further error analysis is provided within the sections following this one.

3.1 SD-1D

The program used throughout this study to simulate the Tokamak edge region was SD-1D (SOL and Divertor in One Dimension), developed by B. Dudson *et al* [24]. SD-1D simulates a plasma fluid interacting with a neutral gas in one dimension (parallel to the magnetic field, $\mathbf{B} = B \cdot \mathbf{b}$). SD-1D models many aspects of this system, including radiative losses and both the advection and conductive transport of energy.

3.1.1 SD-1D Model

SD-1D evolves the density (n), static pressure (p) and parallel momentum density ($m_i n v_\parallel$) of both plasma and neutrals along the SOL. Throughout simulation, isotropic ion and electron temperatures are assumed ($T = T_i = T_e$) and are given in units of eV. To achieve this, equation (5)–(8) are solved.

$$\frac{\partial n}{\partial t} = -\nabla \cdot [\mathbf{b} v_\parallel n] + S_n - S \tag{5}$$

$$\frac{\partial}{\partial t}\left(\frac{3}{2}p\right) = -\nabla \cdot \mathbf{q_e} + v_\parallel \partial_\parallel p + S_E - E - R \tag{6}$$

$$\frac{\partial}{\partial t}(m_i n v_\parallel) = -\nabla \cdot [m_i n v_\parallel \mathbf{b} v_\parallel] - \partial_\parallel p - F \tag{7}$$

$$\mathbf{q_e} = \frac{5}{2} p \mathbf{b} v_\parallel - \kappa_\parallel \partial_\parallel T_e \tag{8}$$

Here, $\partial_\parallel \equiv \mathbf{b} \cdot \nabla$. The external particle source (S_n) is adjusted using a proportional-integral (PI) feedback controller to maintain the inputted value of n_u. An external power source (S_E) inputs energy upstream along a region 10 m in length, at a constant rate. Coupling to neutrals is modelled via the implementation of several quantities: sources and sinks of particles (ionisation & recombination) are represented by S, energy exchange by E, radiative losses by R and frictional forces, resulting from ionisation, recombination and charge exchange, by F.

Another three similar equations are solved for the neutral fluid pressure ($p_n = e n_n T_n$), density (n_n) and parallel momentum ($m_i n_n v_{||n}$). Neutrals are not confined by magnetic fields. Therefore, their velocities can contain a perpendicular component. This cross-field motion contributes to the upstream transport of neutrals within the SOL. To allow the mimicking of this process in a 1D model, a parallel projection of this lateral motion is included in the effective neutral parallel velocity equation,

$$v_n = v_{||n} - \left(\frac{B_\phi}{B_\theta}\right)^2 \frac{\delta_{||} p_n}{\nu m_i n_n} \tag{9}$$

Here, the ratio of toroidal magnetic field (B_ϕ) to poloidal field (B_θ) represents a cross-field neutral diffusion coefficient and is defined by the system geometry. $(B_\phi/B_\theta)^2$ was set to 10 within all testing presented here. ν is a collision frequency including charge exchange, ionisation and neutral-neutral collisions. There is no similar cross-field term included in the calculation of plasma velocity. This is because ions are assumed to be tied to magnetic field lines, whereas neutrals can cross freely.

In order to derive equations (5)–(8), several assumptions were made. For example, equation (8) contains the parallel thermal conductivity coefficient, $\kappa_\parallel = \kappa_0 T^{5/2}$. $\kappa_\parallel$ is determined from the Spitzer-Harm model, in which particle mean free paths ($\lambda_{e,i}$) are assumed to be much shorter than the characteristic length scale of temperature variation [25]. However, at high powers, for example during ELM eruption, this model could potentially break down. Large powers entering the SOL result in increased electron temperatures and, since $\lambda_{e,i} \propto T_{e,i}^2$, $\lambda_{e,i}$ will likely increase with this input power. If this value becomes a significant fraction of the length scale simulated by SD-1D, any $\kappa_\parallel$ value calculated using the Spitzer-Harm model would be too large and, in a real reactor, heat transport would become advection dominated.

For this to become a real problem, $T_{e,i}$ values above $\sim$ 200 eV would have to be present in the SOL [26].

Beyond the Spitzer-Harm assumption, various other simplifications have been made. The cross-sections assumed for the calculation of interaction rates were taken from previous work and are shown in Figure 8. To ensure cross-sections are always calculable, any temperatures below 1 eV are assumed to be 1 eV during calculation. This could pose a potential issue, since detachment can see the Divertor region drop far below 5 eV and, as discussed in section 2.4, radiative heat losses and recombination are important mechanisms during detachment. This could in particular make the investigation of the degree of detachment difficult, as there may be a limit to the level of detachment that SD-1D can reach. Finally, recycled neutrals are assumed to have parallel momentum away from the target corresponding to the Franck-Condon energy (3.5 eV) [27].

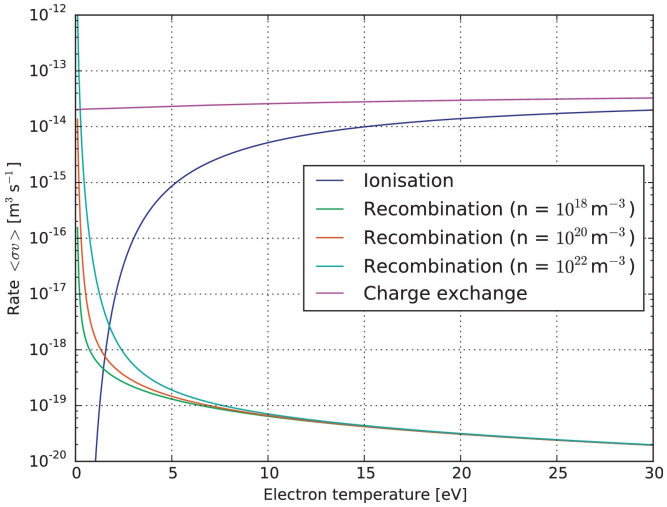

Figure 8. The variation of plasma-neutral interaction cross-sections with electron temperature [28, 29].

3.1.2 Numerical and Computational Methods

The numerical methods employed within SD-1D have been covered in previous work carried out by B. D. Dudson *et al* [24] and therefore will not be discussed in detail here. However, due to the transient nature of the system being modelled, it is important to note the way in which wave propagation is handled by SD-1D. Heat-pulses result in rapid pressure changes and, thus, pressure gradient-driven plasma flux. SD-1D uses a Minmod flux limiting method for the calculation of advection terms of the form $\nabla \cdot [\mathbf{b} v_{||} f]$ [30]. Furthermore, in order to model waves travelling in both directions, this flux is split into two components. This can become computationally expensive but is simplified using the HLL method [31]. This method assumes that the fastest waves in the system travel at the sound speed (v_s), with respect to the flow. Therefore, waves travel with speed $v_{||} + v_s$ or $v_{||} - v_s$. Consequently, supersonic flow is in only one direction but subsonic flow can have multiple directional components.

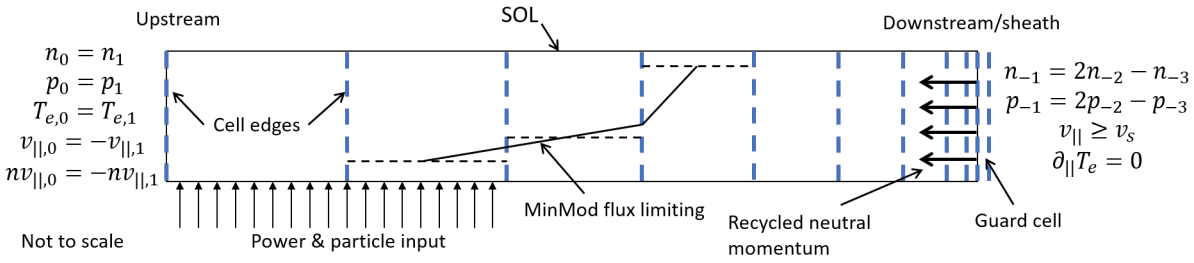

Figure 9. A schematic diagram of the non-uniform mesh of SD-1D with additional features of the program shown, including up and downstream boundary conditions as well as flux limiting. The numerical subscripts within the equations shown represent cell indices.

Figure 9, shows a simple representation of the SD-1D program. Shown at either end of the SOL are the boundary conditions that apply there. At the upstream boundary a zero-flow condition is applied. The method used to enforce this results in the reflection of waves off the upstream boundary. The consequence of this will be discussed in detail below. The downstream boundary conditions enforce the Bohm-Chodura criterion (see section 3.4.2) by switching from a Dirichlet to a Neumann boundary if $v_{||,t} > v_s$. Furthermore, an example of the non-uniform mesh employed by SD-1D is shown in Figure 9. The gradual reduction of downstream cell width reduces computational expense without compromising the accuracy of data gathered. most key process occur downstream in the Divertor region including detachment, recycling, plasma neutral interaction and more. This is the reason for the high downstream mesh resolution.

3.2 Tokamak Simulation

The simulated fraction of ions re-emitted from the target as neutrals was fixed at $f_{recycle} = 0.99$. Once the target becomes saturated with hydrogenic particles, the fraction of ions recycled into neutrals approaches 100%. However, within physical reactors active pumping removes neutral gas from the system. Thus, a $f_{recycle}$ of 0.99 aims to replicate this setup. Although the value of $f_{recycle}$ chosen will effect the system, for example by altering the upstream densities at which flux rollover occurs ($n_{u,rollover}$), the qualitative results observed should remain experimentally relevant.

Beyond $f_{recycle}$, the input parameters required to successfully model the machines , MAST-U and ITER, differ in a number of ways. The most obvious differences are the background power-flux entering the upstream SOL ($Q_{SOL,0} = 50\ MWm^{-2}$ for MAST-U and 270 MWm^{-2} for ITER [32]) and the geometries modelled (length from upstream to downstream - 30 m for MAST-U and 60 m for ITER). However, another key difference is the impurity fraction and species used for each reactor. These were 1% Carbon for MAST-U (calculated by B. D. Dudson *et al* using ADAS data [33]) and 2% Neon for ITER [7].

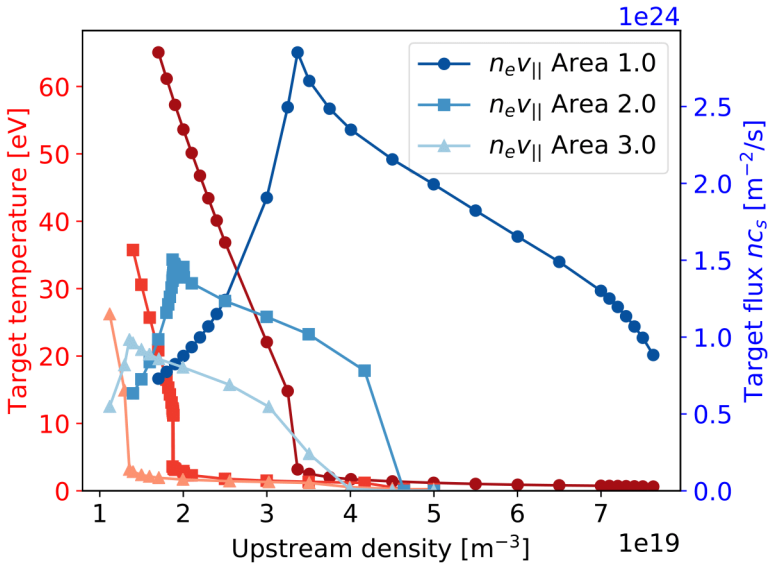

Figure 10. Upstream density scans of target temperature and flux (nc_s) for three different area-expansion factors - 1.0, 2.0 & 3.0. The flux roll-over density moves to lower values for an increased area-expansion. Obtained through a private correspondence with B. D. Dudson.

In order to reliably investigate the impact of the area-expansion factor, A, (ratio of the total field at the X-point to that at the target) on the response of a detached SOL plasma, steady-state solutions displaying equal levels of detachment had to be found for each A value. To permit this, scans of n_u were performed for values of $A = 1.0,\ 2.0$ & 3.0 in the MAST-U case. These simulations were carried out prior to the commencing of this investigation. The results of these scans can be seen in Figure 10. As discussed in section 2.4, The n_u value at which the target flux rolls-over signifies detachment. These roll-over, densities along with the corresponding fixed upstream densities that were chosen for testing

($n_{u,A}$), are shown in Table 1. In order to produce comparable states of detachment, the $n_{u,A}$ values chosen were at consistent percentages above their corresponding $n_{u,rollover}$ value.

Data of the sort shown in Figure 10 was not available for ITER, so a slightly different approach was required. Steady-state ITER solutions were reached, where possible, for each A value with upstream densities far beyond any likely roll-over values. n_u was then fixed to a much lower value and the system allowed to settle back to steady-state. Target temperature (T_t) was then plotted against n_u, showing their variation in time. The plot for $A = 1.0$ displayed a sharp increase in T_t, similar to those of Figure 10, below some value of n_u. Thus, this point of T_t increase was assumed to be the roll-over density. However, for $A = 2.0$ & 3.0, n_u reached a minimum and would not drop below $3.2 \times 10^{19}\ m^{-3}$, posing an issue for this investigation. Several techniques of introducing various perturbations in power and particle flux as well as tuning the PI feedback density controller were tried to attempt to force n_u below the minimum value. However, this limit could not be surpassed. Therefore, to permit a reliable comparison between MAST-U and ITER, it was assumed that,

$$\left(\frac{n_{u,A}}{n_{u,A+1}}\right)_{MAST-U} = \left(\frac{n_{u,A}}{n_{u,A+1}}\right)_{ITER} \tag{10}$$

$n_{u,rollover}$ for $A = 1.0$ is stated in Table 1, along with the densities found using equation (10).

	MAST-U		ITER	
A	$\mathbf{n_{u,rollover}}$	$\mathbf{n_{u,A}}$	$\mathbf{n_{u,rollover}}$	$\mathbf{n_{u,A}}$
1.0	3.3 ± 0.1	3.5	5.2 ± 0.1	5.5
2.0	1.883 ± 0.003	2.0	< 3.2	3.2
3.0	1.34 ± 0.05	1.42	< 3.2	-

Table 1: Roll-over densities ($n_{u,rollover}$) and the fixed upstream densities ($n_{u,A}$) chosen for each area-expansion factor (A) for both MAST-U and ITER. No value of $n_{u,A}$ could be found, for ITER with $A = 3.0$, which resulted in a steady-state solution. Therefore this data could not be collected. All densities are given in units of [10^{19} m^{-3}].

The upstream density was again important in the investigation into the affect of the degree to which the Divertor is detached. There is no clear definition of a 'degree' of detachment. Therefore, using Figure 10, it was assumed that beyond $n_{u,rollover}$, the Divertor becomes more detached with an increasing n_u. This assumption was rooted in the idea that larger densities further reduce λ and, therefore, increase collision frequencies within the SOL. As n_u is raised, the Divertor becomes increasingly opaque to upstream plasma prompting further radiative heat losses and plasma recombination rates. Thus, detachment is enhanced. Figure 11 supports this hypothesis. Using these ideas, with $A = 1.0$, the values tested were $n_u = 3.5 \times 10^{19}\ m^{-3}$ and $5.0 \times 10^{19}\ m^{-3}$ for MAST-U and $n_u = 5.5 \times 10^{19}\ m^{-3}$ and $6.5 \times 10^{19}\ m^{-3}$ for ITER.

3.3 Heat-Pulse Modelling

Before a heat-pulse could be simulated in SD-1D, it was vital to allow the system to settle into steady-state. Without this, the system would evolve with or without a heat-pulse, making the task of discerning between effects of the heat-pulse and the simple evolution of the system difficult. By comparing data from several heat-pulse simulations, all with the same starting scenario, this became apparent. If a change was observed in a parameter such as T_t or $nv_{||,t}$ at the same point in time, independent of heat-pulse length or power, it was deemed that a steady-state solution had not been used as the starting scenario. An example of this can be seen in Figure 12.

Once a steady-state solution had been found, a heat-pulse could be simulated. Firstly, the input upstream power-flux ($q_{||,u}$) was increased and a length of time, much greater than any ELM-length, simulated ($\sim 4\ ms$, in our case). Then, whilst returning the input power-flux to the background level, the simulation was restarted from some point in time along the 'power-on' simulation, thus defining the duration of the pulse. By combining the data from both the 'power-on' and 'power-off' simulations an entire heat-pulse could be formed. This method results in the modelling of input power-flux as a step function. However, the resultant target heat-flux profiles are much more shaped, as shown in Figure 18.

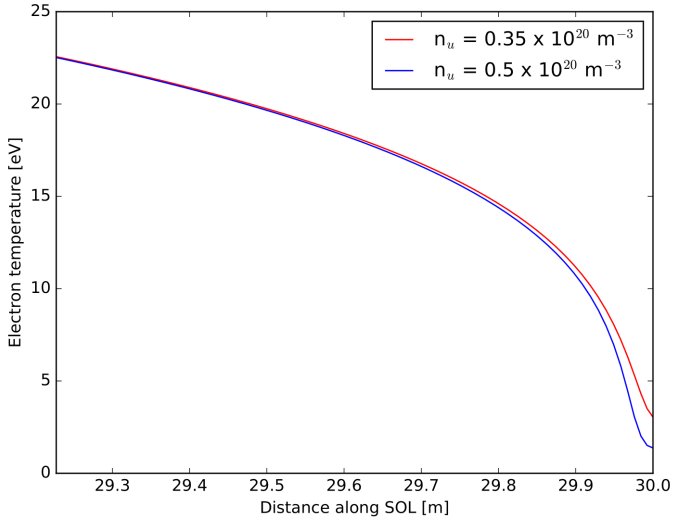

Figure 11. This plot shows the effect of increasing the upstream density on the state of Divertor detachment. As n_u is increased the detached region extends further upstream and the target temperature lowers. Thus, the degree to which the Divertor has detached has increased. The data shown was taken from MAST-U steady-state solutions with $A = 1.0$.

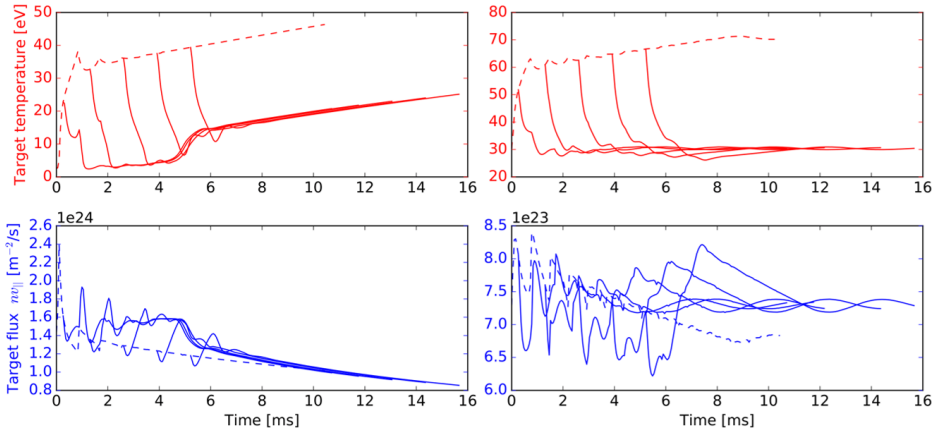

Figure 12. The effect of a steady-state solution, shown for several heat-pulses of double the background power-flux and differing duration. Data is shown for a MAST-U simulation with $A = 2.0$ and $n_u = 1.5 \times 10^{19}\ m^{-3}$. The steady-state solution within this scenario is an attached SOL plasma. Left: Starting scenario has not reach steady-state and is initially detached. Right: Starting from the steady-state solution. The dashed line represents the data taken from the 'power-on' simulation, whereas the solid lines show 'power-off' data. The change displayed in the left-hand side graphs at 5 ms is a result of the attaching of the Divertor plasma and is absent from the graphs on the right. Additionally, the attached nature of the steady-state solutions results in much greater target temperatures compared to the detached starting scenario.

There are several possible limitations of this method. For example, ELMs are unlikely to deposit heat into the SOL in the manner of a step function. A ramp in upstream power is more likely. Furthermore, it has been well established that ELMs do not only increase the power entering the SOL but also the number of particles crossing the separatrix [21]. Despite this, our method does not account for increased particle input. However, the key aim of this investigation is not to produce definitive quantitative estimates of parameters but rather provide a general insight into the response of SOL plasma to heat-pulses. Therefore, it can be said that, although the assumptions of this method may be idealistic, they should produce experimentally relevant results. Therefore, any investigation into the response of plasma to both power and particle transients combined will be left for future study.

3.4 Testing

To ensure the simulations carried out produced reliable and reproducible data, tests of SD-1D and the methods employed were performed. All heat-pulse simulations must be sufficiently resolved in space and time. Therefore, convergence tests were carried out. Furthermore, comparisons between known experimental data and theoretical expectations were performed to ensure the program behaved as expected.

3.4.1 Resolution

Firstly, spatial convergence was tested. To do this several simulations with varying numbers of cells were ran to steady-state. The final values of target density (n_t), temperature and heat-flux for each of these simulations were then plotted against the number of cells simulated. If SD-1D operated as expected, the convergence of these values would be observed as the resolution was increased. This was indeed the case, as shown by Figure 13. To limit program run-time whilst maintaining accuracy, a resolution of ~ 13 cells per metre was used (400 cells for MAST-U and 800 for ITER).

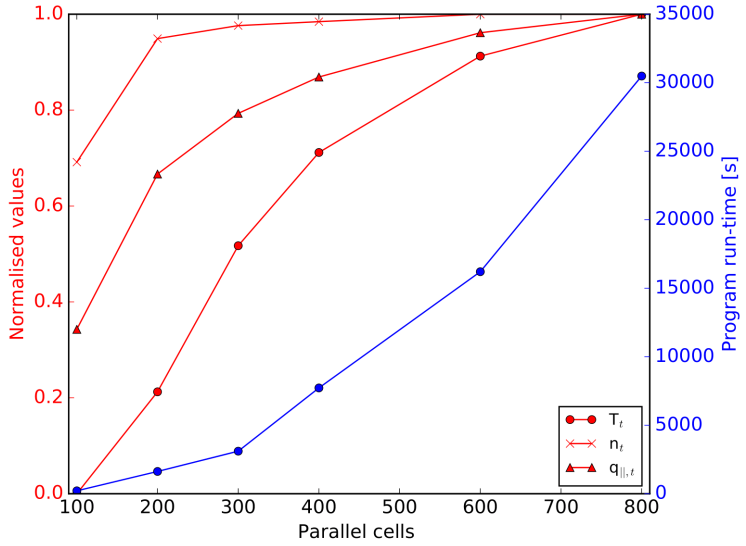

Figure 13. The convergence of several quantities with the increase of spatial resolution within SD-1D for the MAST-U reactor. Also shown is the rapid increase in program run-time. All quantities lie within the acceptable range of a 10% error above 600 cells. However, above 400 cells the program run-time increases rapidly. Therefore, a resolution of 400 cells for MAST-U (equivalent to 800 cells for ITER) was used throughout this study. This resolution permitted the running of the many simulations required for this analysis within the time frame provided.

When probing deeper into the effect of spatial resolution, it became apparent that lowering the resolution caused a shift in the state of Divertor detachment. As shown in Figure 14, a lower resolution (number of cells, NOUT) causes a greater degree of detachment - the upstream movement of the detachment front. This suggests that the lower resolution does not necessarily reduce the reliability of the system being simulated. Instead, the system can simply be regarded as being more detachment. Therefore, preserving reliability with a small expense to accuracy.

The system under investigation throughout this report is dynamic. Therefore, it is key that each simulated heat-pulse is sufficiently resolved in time. The fastest mechanism of heat transfer modelled by SD-1D is conduction. As explained in section 3.1.1, the conductive transport of heat within SD-1D is calculated using the Spitzer-Harm model. Using this model the time-scale for conductive heat transport between the upstream and downstream (τ) can be estimated as,

$$\tau \sim \frac{L_{||}^2}{k_0 T^{\frac{5}{2}}} \tag{11}$$

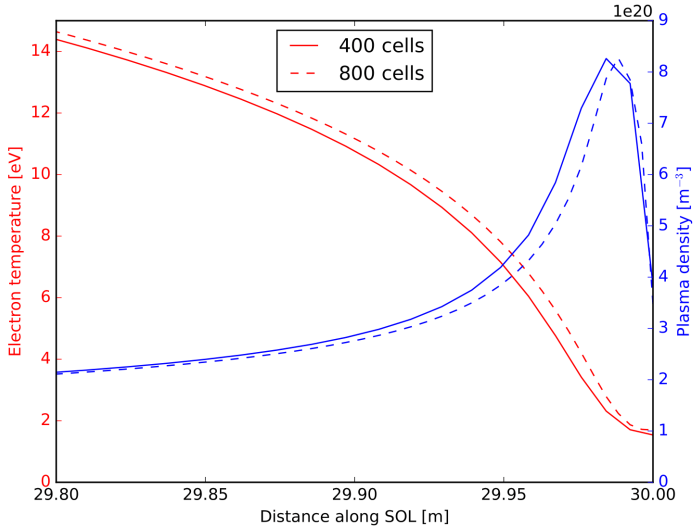

Figure 14. Profiles of plasma temperature and density for two different spatial resolutions.

Since, in the MAST-U case, $L_{||} = 30\ m$, $k_0 \sim 2000$ and the SOL temperature is typically in the range of $5 - 100eV$, $\tau \sim 0.05\ ms$. Consequently, the resolution chosen for heat-pulse simulation was $0.0107\ ms$ (a time-step of 500 in the SD-1D input file).

3.4.2 The Two-point Model

The 2PM is a simple model used to relate upstream values on individual flux tubes (surrounding magnetic field lines), such as n_u and upstream temperature (T_u), to their corresponding values downstream at Divertor targets. To achieve this, equations (12)-(14) are used alongside input values of the power entering the upstream SOL (q) and n_u. These equations are a consequence of particle, pressure and power balance (see section 5.2 of [2]).

$$2n_t T_t = n_u T_u \tag{12}$$

$$T_u^{\frac{7}{2}} = T_t^{\frac{7}{2}} + \frac{7}{2}\frac{qL}{\kappa_{0e}} \tag{13}$$

$$q = q_t = \gamma n_t k T_t c_{st} \tag{14}$$

To allow the reduction of SD-1D's more complex equations to that of (12)-(14), several assumptions are made:

1. Cross field particle transport is ignored. Including that, during recycling, all ions impinge the target recombine and are re-ionised along the same flux tube.
2. All plasma is assumed to be stagnant, apart from that which sits in the recycling region.
3. Total pressure is assumed to be constant along a flux tube of length L.
4. No power is lost along an individual flux tube. Therefore, the power entering upstream must equal the power reaching the target (q_t).
5. The only mechanism of heat transport is assumed to be conduction, with a parallel electron conductivity coefficient k_{0e} and sheath heat transmission coefficient γ.
6. The designated upstream location is the only heat source along a flux tube. Similarly, the target is the only heat sink.

7. Finally, the Bohm–Chodura criterion, described in [34], provides the boundary condition for the 2 point model at the target: ion velocity at target (v_t) must be at least sonic, $v_t \geq v_{s,t}$.

So long as the above assumptions hold within the system simulated by SD-1D, the 2PM can provide a theoretical foundation from which SD-1D can be validated. SD-1D has previously been tested against a modified version of the two-point model in which momentum (f_{mom}) and power (f_{pow}) loss fractions are included along flux tubes. The results of this benchmark are shown in Table 2. For attached plasma (below flux roll-over) SD-1D showed good agreement with the modified 2PM.

n_u [$\times 10^{19}$ m^{-3}]	Relative error [%]	f_{mom}	f_{pow}
1.8	0.003	0.22	0.25
1.9	2	0.73	0.78
3.0	10	0.73	0.92
4.0	80	0.87	0.98

Table 2: The comparison of SD-1D results against a modified 2PM as a function of upstream density. A was set to 2.0. Therefore, rollover occurs $\sim 1.9 \times 10^{19}$ m^{-3}. Data presented was taken from [24].

3.4.3 Comparing to Previous Work

Comparisons between SD-1D and other one-dimensional simulations were carried out. The profiles of various parameters including the density, temperature and pressure of both plasma and neutrals within a detached state, produced with SD-1D, are shown below in Figure 15. The distributions shown match the typical profiles of a detached SOL plasma which have been reproduced on multiple occasions, by different one-dimensional codes [35, 36, 37]. Therefore, it can be concluded that SD-1D is capable of correctly simulating a detached Divertor plasma.

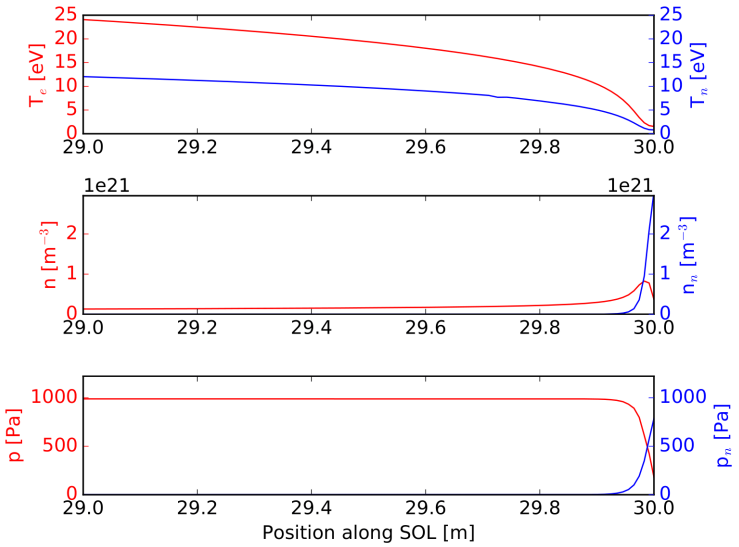

Figure 15. The profiles of temperature (T), density (n) and pressure (p) for both plasma and neutrals with a detached Divertor. Shown is only a small distance in front of the target plate of a MAST-U like SOL geometry. The sharp reductions in plasma pressure and temperature in front of the target, along with the density peaks observed there, indicate a detached plasma state.

4 Results

Within this section the results gathered using the methods stated above are presented. Furthermore, some discussion of the potential implications of what has been observed will be provided. Particular emphasis will be placed upon the qualitative relationships observed between parameters such that conclusions remain within the limits of the assumptions applied.

4.1 Heat-pulse Driven System Evolution

This sub-section will attempt to detail the evolution of the plasma-neutral fluid in response to a pulse of heat. Firstly, the energy dumped upstream is conducted downstream to the target. Sound waves are the next fastest mechanism of information transfer. Thus, one would expect the arrival of a sound wave to follow any conducted heat. However, there is another key feature observed when simulating a pulse of heat entering the upstream SOL.

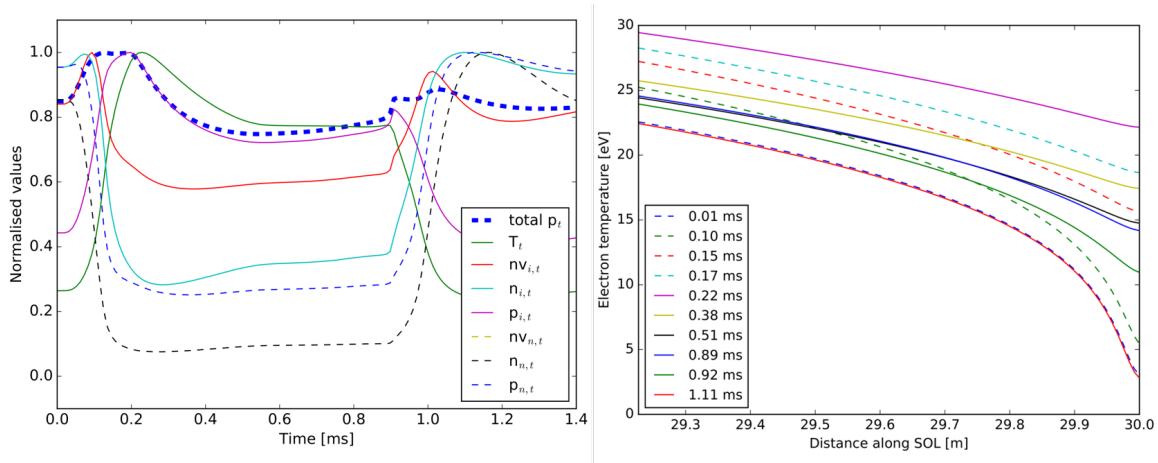

Figure 16. The evolution of plasma parameters at the Divertor target resulting from a heat-pulse of duration 0.17 ms and power twice that of the background. The impact of a sound wave can be seen most prominently in the profiles of plasma flux ($nv_{i,t}$), plasma pressure ($p_{i,t}$) and the total pressure (p_t) around ~ 0.9 ms. The dashed lines of each graph indicate different things - right: properties of the neutral fluid, left: times during the pulse input.

Figure 16 shows the response of the plasma-neutral mix to the input of a heat-pulse. Within the time-scale of conductive heat transport (~ 0.05 ms), the system begins to change. The arrival of this conducted heat is likely to ionise many neutrals close to the target. If this is correct then a reduction in neutral density at the target ($n_{n,t}$) and a corresponding increase in n_t should be observed. $n_{n,t}$ does indeed reduce within a small time frame by approximately 75% of its original value and an increase in n_t is initially present. However, this is not sustained and n_t quickly begins to decrease significantly. This may seem contradictory but is the result of an increase in dynamic pressure close to the target. The sudden ionisation of the neutral fluid results in the rapid (< 0.15 ms) re-attachment of the Divertor (shown in the temperature profiles of Figure 16) and increases the flow of plasma to the target. The consequent change in dynamic plasma pressure ($m_i n v_{||}^2$) quickly increases the total pressure of the plasma-neutral mix close to the target. The target density peak is then re-distributed in an attempt to minimise pressure gradients. However, the particles are limited to the sound speed, preventing plasma flow from equalising this pressure before the increase occurs. As a result, a secondary sound wave (additional to any primary upstream wave) is observed propagating away from the target, as shown in Figure 17.

For this simulation, v_s was averaged in time and along the length of the SOL. The value calculated was $v_s = 63 \pm 1$ kms^{-1}. Thus, within MAST-U, the primary sound wave should arrive at the target after 0.476 ± 0.007 ms. After almost exactly this length of time, a slight increase in n_t and $nv_{i,t}$ is observed. Therefore, this must correspond to the primary wave. However, after twice this time a much greater increase is observed. This peak corresponds to the return of the secondary wave to the target. Since this wave needed to travel the length of the SOL twice, it makes sense that it should arrive at this time. Please note, the continued rise in all parameters observed soon after is not a result of this waves return. Instead, this appears to be the re-detaching of the Divertor. Furthermore, the second peak in $nv_{i,t}$ at

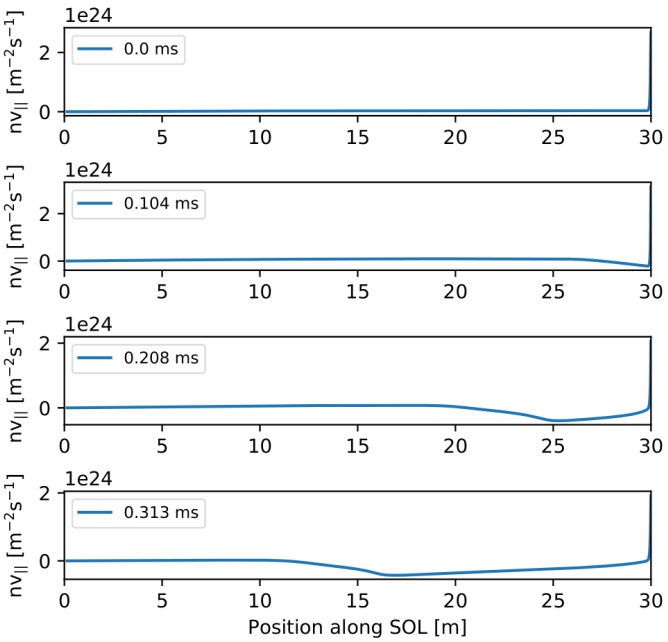

Figure 17. The profile of $nv_{||}$ along the SOL during a heat-pulse. A wave can be seen originating from in front of the target and propagating upstream.

this time is not believed to be the result of a wave but instead the delay between increased recycling due to neutral build-up and the onset of detachment.

Following the secondary waves return, the system transitions back into its original state. However, prior to this, the systems evolution appears to slow. This is particularly apparent in the left hand graph of Figure 16. Therefore, it could be argued that the return of the secondary wave aids to push the system back into a detached state. The sudden compression brought on by the return of the secondary wave will result in an increased density and a consequent reduction in target temperature. As shown in Figure 8, a reduction in temperature corresponds to a decrease in the rate of ionisation as well as an increase in the rate of recombination. Therefore, provided that pulse energy is no longer entering upstream, the temperature decrease caused by this wave could begin a run away cooling effect as more neutrals radiate energy from the system. It should be made clear that the secondary wave is not believed to be the primary cause of re-detachment but instead provides only a perturbation which speeds up the processes. Nevertheless, the propagation of strong secondary waves could play an important role in the re-detaching of the Divertor following a heat-pulse such as an ELM.

Considering the apparent role of the secondary waves, it is important to question how realistic they are and within what system could they be observed. To return to the target the secondary wave must be reflected from the upstream boundary. The boundary conditions enforced within this model ensure that this is the case. Yet, the SOL of a physical Tokamak does not have a zero flow boundary condition applied to it and waves are free to pass through this boundary. Thus, any propagating waves would likely dissipate much of their energy before returning to the target. With this, it is possible that the role of the secondary wave is exaggerate by the model. However, there is a system in which these secondary waves could appear as if reflected from the upstream boundary. A dual Divertor setup should result in two counter propagating sound waves. These waves would pass somewhere along the SOL and appear as if reflected from the point of view of either Divertor. Fortunately, MAST-U incorporates this dual Divertor design and is a good candidate for the type of Tokamak this model could be applied to.

4.2 Heat-pulse Energy Dissipation

To understand the effect of a heat-pulse entering the SOL it is important to determine how the heat contained in the pulse is lost within this region. As stated in section 2.3 there are several mechanisms by which this heat can be lost. Furthermore, the amount of energy lost to each specific channel changes depending on the state of the plasma. As the plasma simulated here is initially detached, a significant

fraction of the externally inputted energy is either lost to radiation or transferred to the neutral fluid. However, the heat-flux to the target surface remains the dominant energy transfer channel. Within this section the changes to the respective flow of energy through these various channels will be analysed.

The energy data presented in this section was calculated through the integration of the various energy fluxes (target heat-flux, radiative losses, etc) and therefore represent energy densities (Jm^{-2}). To permit this a very simple numerical integration method was employed. Each curve to be integrated was divided into the smallest time segments possible. This is given by the simulation resolution ($dt = 0.0107\ ms$). The total area of each segment was then combined to give the area under the curve. An example of this sort of integration is shown in Figure 18. What can also be seen is the small scale of errors resulting from this method of integration. Hence, for most cases, this error can be ignored. However, as the pulse duration is decreased these errors could become large due to the reduced number of segments.

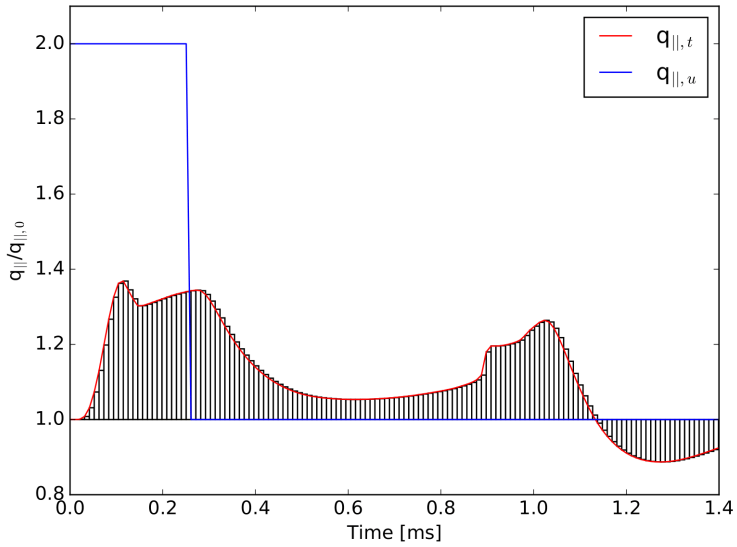

Figure 18. The variation in both the target ($q_{||,t}$) and input ($q_{||,u}$) heat-flux for a pulse lasting 0.26 ms at twice the background input power ($q_{||,u,0}$). Also shown is an example of the simple rectangular integration method used to determine the total deposited energy density during a pulse. The initial peak caused by sudden re-attachment can also be seen at 0.1 ms as well as the return of the secondary wave around 0.9 ms

Figure 19 suggests that, for certain pulse powers and durations, the change in the energy density deposited at the target (ΔQ_t) can be around four and a half times that which is inputted upstream (ΔQ_{SOL}). The target heat-flux was calculated as a combination of plasma thermal energy ($\gamma n v_{||} T$) and the energy released through surface recombination ($E_{rec} = 15.8\ eV$, see section 2.1). The appearance of this additional heat suggests that energy which, prior to the pulse, would have been lost to a mechanism, such as radiative emission, is now directly impinging on the Divertor target. This hypothesis would also explain the reduction in the deposited fraction as pulse power and duration are increased. As the energy contained within a pulse becomes much greater than that which was once lost to other mechanisms, the influence of the pulse energy would become dominant and the curve should tend towards one, as is the case in Figure 19.

To determine the loss mechanism from which this additional energy has been taken, plots similar to that of Figure 19 were produced for several loss mechanisms. Figure 20 suggest that the main cause of the increased deposition fraction is the decrease in radiative emission from electron neutral excitation (ΔR_{ex}). As neutrals are ionised by the heat-pulse, the rate of electron neutral interaction will decrease. Thus, reducing the energy lost through this mechanism. Furthermore, the sum of the impurity radiation losses (ΔR_{imp}) with ΔR_{ex} matches that of ΔQ_t. This solidifies the idea that the increased energy deposition on the target is caused by the transfer of energy flow from loss mechanisms to target heat-flux.

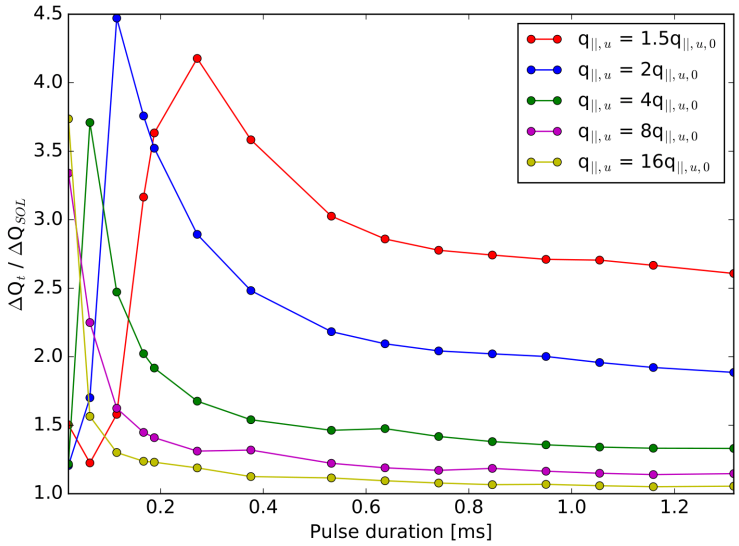

Figure 19. The fraction of pulse energy which reaches the target as a function of pulse duration and magnitude. $\Delta Q_t/\Delta Q_{SOL}$ defines the energy density, above background, that is deposited onto the target (ΔQ_t) as a fraction of the energy density, above background, contained within the upstream pulse (ΔQ_{SOL}). All simulations which comprise the source of this data were ran using MAST-U inputs with $A = 1.0$.

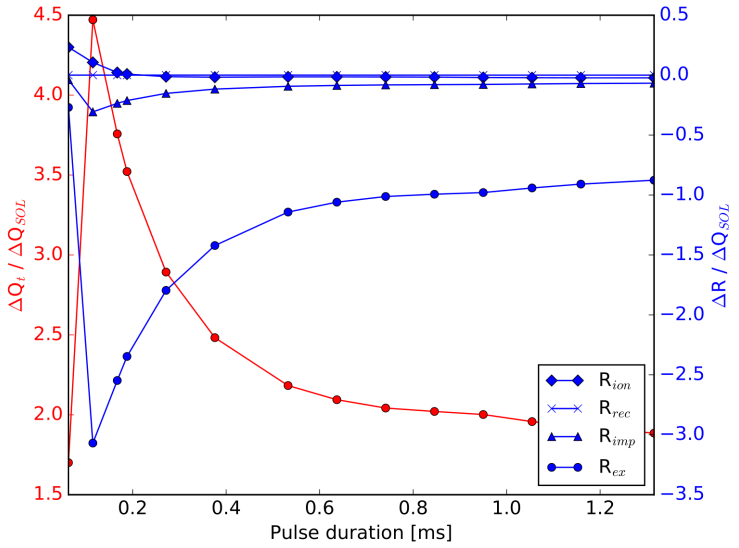

Figure 20. The change in radiative losses (ΔR) resulting from a heat-pulse. Data shown was taken from a pulse with power-flux twice the background input ($q_{||,u} = 2q_{||,u,0}$) on MAST-U with $A = 1.0$. The fraction of pulse energy deposited onto the target is also shown for comparison.

4.3 Target Heat-Loads

To determine the scale of a heat-pulse's power-flux to target surfaces, $\Delta E/\sqrt{t}$ was calculated for several different pulses. t was defined as the time take for $q_{||,t}$ to drop below its background value after the initial rise. ΔE was then defined as the area under the $q_{||,t}$ curve during this time and was calculated using the numerical integration method described in section 4.2. As previously stated, reducing the duration of the heat-pulse can result in an increased error for ΔE. However, this error remains a minute fraction of the total area because of the inclusion of the background flux. Thus, errors in $\Delta E/\sqrt{t}$ were considered negligible. As the duration of a pulse is increased, the total energy inputted increases proportionally. Therefore, if the method of defining t is effective, one would expect to see the relationship $\Delta E/\sqrt{t} \propto \sqrt{t}$.

This is indeed observed, as shown in Figure 21. Furthermore, the measured $\Delta E/\sqrt{t}$ values of long duration pulses diverge from the direct deposition cases. This is likely to be a result of the extended target deposition times, an example of which is shown in Figure 18.

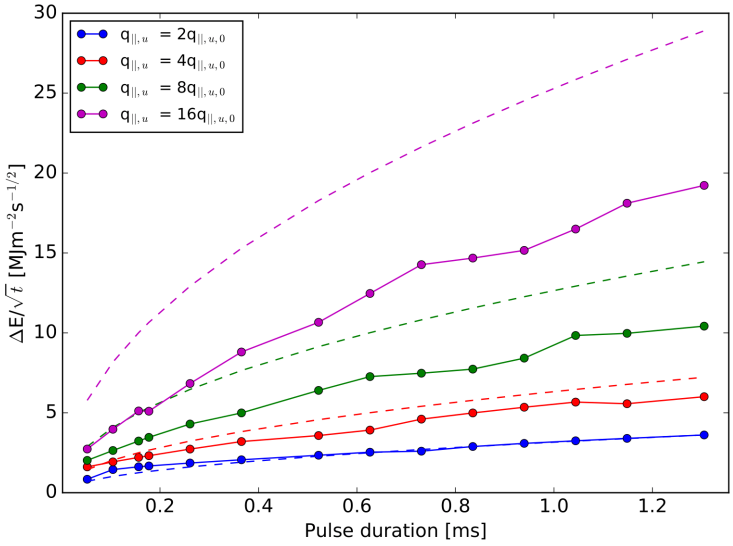

Figure 21. The variation of $\Delta E/\sqrt{t}$ with heat-pulse duration and magnitude. Also shown are the curves corresponding to directly depositing the pulse energy onto the target within its duration (dashed lines). In some low duration cases, $\Delta E/\sqrt{t}$ was seen to exceed the direct case, in agreement with the results presented in section 4.2.

The $\Delta E/\sqrt{t}$ curves, shown in Figure 21, do not cross the damage thresholds stated in Section 2.3. This is a positive prospect as it seems MAST-U will be free from excessive Divertor target damage due to heat-pulses of the kind simulated here. However, this may not be the case for larger reactors. As previously stated, ITER is expected to produce ELMs of vastly greater energy. Therefore, it is important to understand the effectiveness of heat-load mitigation methods on all machines if the most effective techniques are to be revealed.

4.3.1 Damage Mitigation Methods

As described in section 3, two methods of reducing heat-loads were tested - expanding the magnetic flux area close to the target and increasing n_u. However, a problem was encountered when carrying out these investigations. Highly detached simulations (high n_u and some A values) resulted in extreme parameter gradients further from the target. Because of the non-uniform mesh of SD-1D, the spatial resolution further from the target is reduced. Consequently, these gradients became poorly resolved and lead to computational instabilities and unusable data. This limited the degree of detachment achievable with chosen resolution and was most prominent within simulations of ITER.

Increasing A was found to reduce the power-loads to Divertor targets in accordance with the increased area over which the power is spread. Figure 22 shows that, once adjusted for flux expansion, the $\Delta E/\sqrt{t}$ curves of different A values are near identical above $q_{||,u} = 4 \cdot q_{||,u,0}$. However, below this pulse magnitude the values begin to diverge. This is because, for these pulses, more power is lost through radiative emission as shown in the right hand graph of Figure 22. This suggests that expanding the flux area has an effect additional to simply spreading power over a larger area. Since radiative losses are maintained at higher levels, raising A appears to increase the retention of neutral fluid.

The graphs of Figure 22 also show the impact of increasing n_u. It can be seen that, for low pulse powers, a larger n_u value can drastically reduce the target heat-load. Furthermore, the transfer of power from radiative losses to target heat-loads is reduced. From this, it can be concluded that an increased degree of detachment provides better protection for target surfaces. However, this is not a result of pulse power being radiated but instead the simple maintenance of radiative losses already occurring prior to the pulse. Thus, a denser upstream plasma produces a more robust state of detachment.

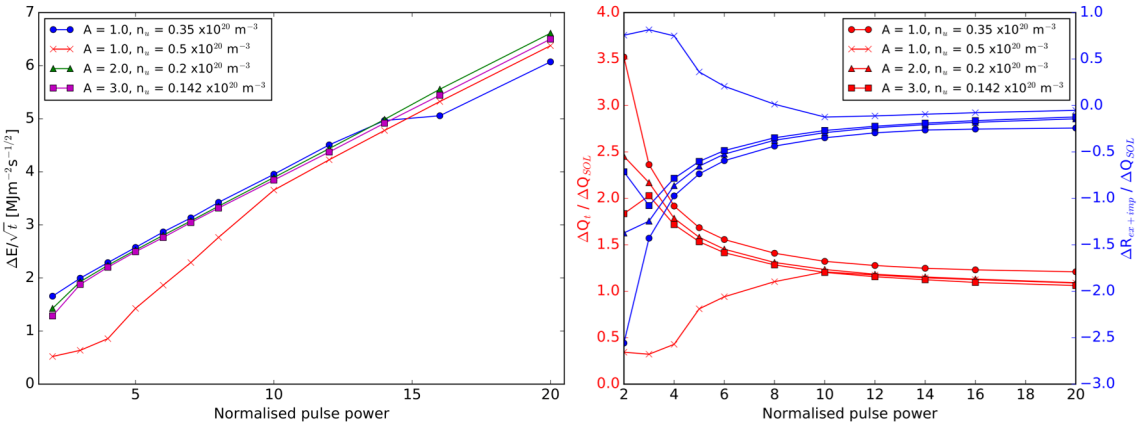

Figure 22. Left: The change in $\Delta E/\sqrt{t}$ with pulse power-flux (normalised to $q_{||,u,0}$) for pulses of duration 0.17 ms. Also shown is the effect of increasing both A and n_u. Right: The change in the target power-loads and radiative losses for the same scan of pulses. Note: each curve has been multiplied by their respective area expansion factors.

4.4 Extending to ITER

Now that we have built a picture of MAST-U's response to heat-pulses, we can extend this investigation to ITER. However, when modelling ITER, several problems were encountered. As discussed in section 3.2, a minimum value of $n_u = 3.2 \times 10^{20}\ m^{-3}$ was reached. Consequently, the only steady-state solutions achievable for increased A values were at a much greater levels of detachment than had previously been simulated for MAST-U. Figure 23 shows this increased state of detachment. As stated in section 4.3.1, highly detached states with strong upstream gradients result in unstable solutions. Thus, a reliable investigation into the effect of area expansion within ITER was not achievable with this method. However, investigation into the effect of increasing n_u was.

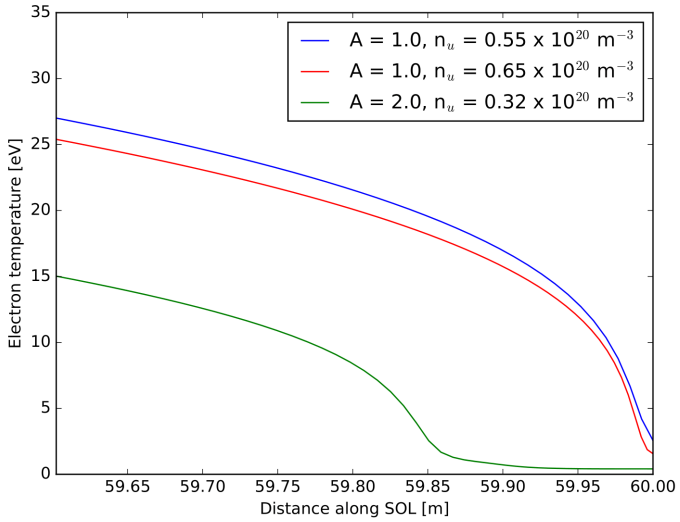

Figure 23. The temperature profiles of ITER edge plasma close to the target for several A and n_u values. The increased detachment present in the $A = 2.0$ case can be seen as the upstream location of the rapid temperature drop.

Increasing n_u was found to have a similar effect within ITER compared to that of MAST-U. Figure 24 shows little difference between the two densities above a pulse magnitude of four times the background. However, below this, dissimilarities between radiative losses were observed. A higher upstream density was shown to increase the energy lost to radiation. Therefore, the loss mechanisms within ITER respond to a heat-pulse in a similar way to that of MAST-U. Furthermore, the heat-loads calculated for ITER

appear to be five times that of MAST-U, but still within acceptable values. However, pulse powers above those simulated here would likely exceed damage thresholds.

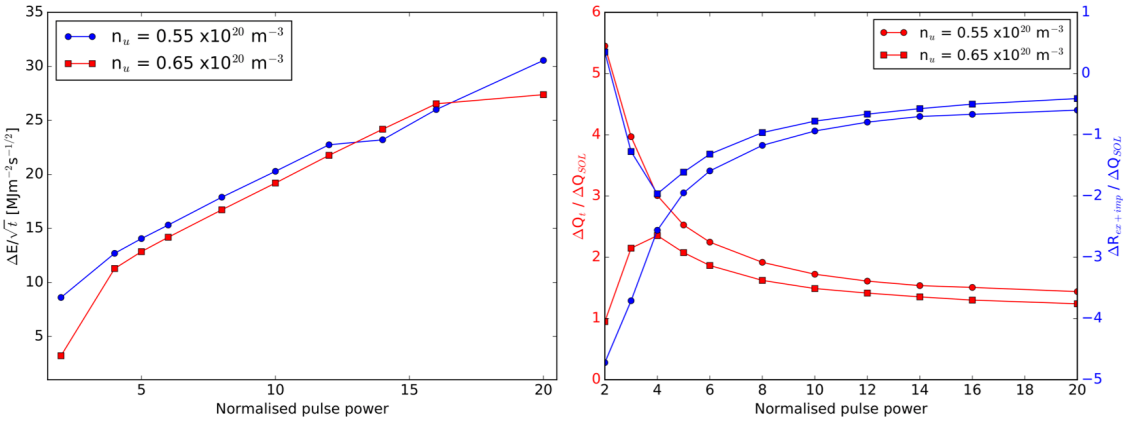

Figure 24. Left: The calculated heat-loads for ITER as a function of pulse power. Right: The change in target power-loads and radiative losses as the power of a 0.17 ms pulse is increased for ITER. All data shown was taken with an area expansion of $A = 1.0$.

5 Conclusions

This report has presented an investigation of the response of detached SOL plasma to transient heat-pulses through the use of a 1D plasma-neutral fluid code. Many assumptions were required to permit the modeling of specific plasma states and Tokamak reactors. This is likely to limit the accuracy of reactor specific quantitative data. However, generic relationships and key observations remain experimentally relevant. Thus, the key conclusions of this report will focus on the qualitative trends and the system evolution observed. Specific quantitative outcomes will then be commented on within the limit of accuracy permitted by the model.

Firstly, The evolution of the plasma-neutral mix in response to a heat-pulse was investigated. Conductive heat transport was found to rapidly deplete the neutral fluid. Furthermore, The attaching of the divertor lead to changes in pressure which forced the re-distribution of plasma and, in some cases, produces a high amplitude sound wave at the target. Thus, the detection of these waves should act as an indicator of heat-pulse-driven Divertor re-attachment. The observation of this propagating front could be achieved through measurements of plasma emission spectra within the SOL [38].

Another key observation of this report was that the energy deposited onto target surfaces can rise above that contained within a heat-pulse. This is a result of the transfer of power-flux from radiative losses to target heat-flux. Therefore, a measurement of ELM-driven target power-loads could potentially include this transferred power and overestimate the energy crossing the separatrix during an ELM. Investigation into the fraction of ELM energy reaching the target was carried out by A. Kirk *et al* [23] on MAST using equilibrium fitting. This suggested a reduced fraction of ELM energy is deposited onto target surfaces. However, this was demonstrated on an attached plasma and, therefore, does not necessarily contradict the findings of this report. The sort of methods used by Kirk could be applied to a detached system in order to test this reports findings within a physical Tokamak.

With a comparable degree of detachment on MAST-U and ITER, the power-loads present in the ITER case were around fives times that of MAST-U. The background input power-flux used to simulate ITER was 5.4 times that of MAST-U. Thus, the power-loads induced onto target surfaces by ELMs appear to increase proportionally with the power-flux crossing the separatrix prior to any ELM-burst and, therefore, with the power stored in the plasma core. Furthermore, increasing the upstream density, and thus the degree of detachment, strengthened the Divertors ability to maintain neutral and impurity radiative losses. This conclusion was reached for both MAST-U and ITER. Additionally, for MAST-U, the energy density deposited onto target surfaces by a heat-pulse was found to be inversely proportional to A. Moreover, for low energy pulses, increasing A limited the reduction in radiative losses caused by a heat-pulse. Therefore, expanding the magnetic flux area appears to aid in the retention of neutral fluid.

Thus, the Super-X Divertor design may have multiple benefits. This observation could not be confirmed on the ITER reactor due to the spatial resolution used. To permit the modelling of ITER with area expansion enabled, simulations with a higher spatial resolution should be ran in the future.

This report has presented a method of simulating heat-pulses using the 1D plasma-fluid code SD-1D. The results found have provided an insight into the response of a detached Tokamak Divertor to transient heat-bursts. Finally, this method has also allowed the analysis of key damage mitigation methods and demonstrated their promising effectiveness.

Acknowledgements

I would like to acknowledge the help of my supervisor Dr B. D. Dudson[1]. I could not have achieved what I have without his guidance.

References

[1] Joe Milnes et al. Mast upgrade – construction status. *Fusion Engineering and Design*, 96-97:42 – 47, 2015. Proceedings of the 28th Symposium On Fusion Technology (SOFT-28).

[2] Peter C Stangeby. *The Plasma Boundary of Magnetic Fusion Devices*. Taylor & Francis Group, 2000.

[3] A Loarte et al. Chapter 4: Power and particle control. *Nuclear Fusion*, 47(6):S203–S263, jun 2007.

[4] N. Fedorczak et al. Width of turbulent sol in circular plasmas: A theoretical model validated on experiments in tore supra tokamak. *Nuclear Materials and Energy*, 12:838 – 843, 2017. Proceedings of the 22nd International Conference on Plasma Surface Interactions 2016, 22nd PSI.

[5] J. Davis et al. Radiative cooling of tokamak plasmas due to multiply-charged fe impurity ions. *Journal of Quantitative Spectroscopy and Radiative Transfer*, 17(2):139 – 147, 1977.

[6] G. Janeschitz et al. Divertor performance on carbon and beryllium targets in jet. *Journal of Nuclear Materials*, 196-198:380 – 385, 1992. Plasma-Surface Interactions in Controlled Fusion Devices.

[7] ITER Physics Basis Editors, ITER Physics Expert Group Chairs an Co-Chairs, ITER Joint Central Team, and Physics Unit. Chapter 1: Overview and summary. *Nuclear Fusion*, 39(12):2137–2174, dec 1999.

[8] H Kubo et al. Spectroscopic study of radiative losses in the JT-60U divertor plasma. *Plasma Physics and Controlled Fusion*, 37(10):1133–1140, oct 1995.

[9] S.I. Krasheninnikov et al. Plasma-neutral gas interaction in a tokamak divertor: Effects of hydrogen molecules and plasma recombination. *Journal of Nuclear Materials*, 241-243:283 – 287, 1997.

[10] R.A. Pitts et al. Physics basis for the first ITER tungsten divertor. *Nuclear Materials and Energy*, 20:100696, 2019.

[11] M. Groth et al. Divertor plasma conditions and neutral dynamics in horizontal and vertical divertor configurations in jet-ILW low confinement mode plasmas. *Journal of Nuclear Materials*, 463:471 – 476, 2015. Plasma-Surface Interactions 21.

[12] W. L. Hsu et al. Experimental simulation of the gaseous tokamak divertor. *Phys. Rev. Lett.*, 49:1001–1004, Oct 1982.

[13] F. Alladio et al. The regime of enhanced particle recycling in high density tokamak discharges in the frascati torus. *Physics Letters A*, 90(8):405 – 409, 1982.

[14] S. I. Krasheninnikov and A. S. Kukushkin. Physics of ultimate detachment of a tokamak divertor plasma. *Journal of Plasma Physics*, 83(5):155830501, 2017.

[15] A W Leonard. Plasma detachment in divertor tokamaks. *Plasma Physics and Controlled Fusion*, 60(4):044001, feb 2018.

[16] J. A. Goetz et al. Comparison of detached and radiative divertor operation in alcator c-mod. *Physics of Plasmas*, 3(5):1908–1915, 1996.

[17] S. I. Krasheninnikov et al. Divertor plasma detachment. *Physics of Plasmas*, 23(5):055602, 2016.

[18] B. Lipschultz et al. Divertor physics research on alcator c-mod. *Fusion Science and Technology*, 51(3):369–389, 2007.

[19] F. Wagner et al. Regime of improved confinement and high beta in neutral-beam-heated divertor discharges of the asdex tokamak. *Phys. Rev. Lett.*, 49:1408–1412, 11 1982.

[20] J. W. Hughes et al. High-resolution edge thomson scattering measurements on the alcator c-mod tokamak. *Review of Scientific Instruments*, 72(1):1107–1110, 2001.

[21] A. W. Leonard. Edge-localized-modes in tokamaks. *Physics of Plasmas*, 21(9):090501, 2014.

[22] T Eich et al. Power deposition measurements in deuterium and helium discharges in jet mkiigb divertor by IR-thermography. *Journal of Nuclear Materials*, 313-316:919 – 924, 2003. Plasma-Surface Interactions in Controlled Fusion Devices 15.

[23] A Kirk et al. ELM characteristics in MAST. *Plasma Physics and Controlled Fusion*, 46(3):551–572, feb 2004.

[24] B D Dudson et al. The role of particle, energy and momentum losses in 1d simulations of divertor detachment. *Plasma Physics and Controlled Fusion*, 61(6):065008, may 2019.

[25] Lyman Spitzer. *Physics of fully ionized gases; 1st ed.* Internat. Sci. Tracts Phys. Astron. Interscience, New York, NY, 1956.

[26] J T Omotani and B D Dudson. Non-local approach to kinetic effects on parallel transport in fluid models of the scrape-off layer. *Plasma Physics and Controlled Fusion*, 55(5):055009, apr 2013.

[27] Makoto NAKAMURA et al. One-dimensional time dependent analysis of the detachment front in a divertor plasma: Roles of the cross-field transport. *Plasma and Fusion Research*, 6:2403098–2403098, 2011.

[28] E Havlíčková et al. Benchmarking of a 1d scrape-off layer code SOLF1d with SOLPS and its use in modelling long-legged divertors. *Plasma Physics and Controlled Fusion*, 55(6):065004, may 2013.

[29] B. Dudson et al. Simulation of the interaction between plasma turbulence and neutrals in linear devices. *Nuclear Materials and Energy*, 12:994 – 998, 2017. Proceedings of the 22nd International Conference on Plasma Surface Interactions 2016, 22nd PSI.

[30] Randall LeVeque. *Finite Difference Methods for Ordinary and Partial Differential Equations: Steady-State and Time-Dependent Problems (Classics in Applied Mathematics Classics in Applied Mathemat)*. Society for Industrial and Applied Mathematics, USA, 2007.

[31] Amiram Harten et al. On upstream differencing and godunov-type schemes for hyperbolic conservation laws. *SIAM Review*, 25(1):35–61, 1983.

[32] E Havlíčková et al. Investigation of conventional and super-x divertor configurations of MAST upgrade using scrape-off layer plasma simulation. *Plasma Physics and Controlled Fusion*, 56(7):075008, may 2014.

[33] H. P. Summers. The adas user manual, version 2.6. *http://www.adas.ac.uk/*, 2004.

[34] P. C. Stangeby. The bohm–chodura plasma sheath criterion. *Physics of Plasmas*, 2(3):702–706, 1995.

[35] Makoto NAKAMURA et al. One-dimensional time dependent analysis of the detachment front in a divertor plasma: Roles of the cross-field transport. *Plasma and Fusion Research*, 6:2403098–2403098, 2011.

[36] Rajiv Goswami et al. One-dimensional model of detached plasmas in the scrape-off layer of a divertor tokamak. *Physics of Plasmas*, 8(3):857–870, 2001.

[37] Shinji Nakazawa et al. One-dimensional simulation on stability of detached plasma in a tokamak divertor. *Plasma Physics and Controlled Fusion*, 42(4):401–413, mar 2000.

[38] Paul Heinrich et al. Self-sustained divertor oscillations in asdex upgrade. *Nuclear Fusion*, 2020.